Highly efficient photosynthesis of hydrogen peroxide in ambient conditions

Yu-Xin Ye[a] , Jinhui Pan[a] , Fangyan Xie[b] , Li Gong[b], Siming Huang[c] , Zhuofeng Ke[d], Fang Zhu[a], Jianqiao Xu[a] , and Gangfeng Ouyang[a,e,f,1]

[a]Ministry of Education (MOE) Key Laboratory of Bioinorganic and Synthetic Chemistry, School of Chemistry, Sun Yat-sen University, 510275 Guangzhou, China; [b]Instrumental Analysis and Research Center, Sun Yat-sen University, 510275 Guangzhou, China; [c]Department of Radiology, Sun Yat-sen Memorial Hospital, Sun Yat-sen University, 510275 Guangzhou, China; [d]School of Materials Science and Engineering, Sun Yat-sen University, 510275 Guangzhou, China; [e]Guangdong Provincial Key Laboratory of Emergency Test for Dangerous Chemicals, Guangdong Institute of Analysis (China National Analytical Center Guangzhou), 510070 Guangzhou, China; and [f]Chemistry College, Center of Advanced Analysis and Gene Sequencing, Zhengzhou University, 450001 Zhengzhou, China

Photosynthesis of hydrogen peroxide (H_2O_2) in ambient conditions remains neither cost effective nor environmentally friendly enough because of the rapid charge recombination. Here, a photocatalytic rate of as high as 114 $\mu mol \cdot g^{-1} \cdot h^{-1}$ for the production of H_2O_2 in pure water and open air is achieved by using a Z-scheme heterojunction, which outperforms almost all reported photocatalysts under the same conditions. An extensive study at the atomic level demonstrates that Z-scheme electron transfer is realized by improving the photoresponse of the oxidation semiconductor under visible light, when the difference between the Fermi levels of the two constituent semiconductors is not sufficiently large. Moreover, it is verified that a type II electron transfer pathway can be converted to the desired Z-scheme pathway by tuning the excitation wavelengths. This study demonstrates a feasible strategy for developing efficient Z-scheme photocatalysts by regulating photoresponses.

hydrogen peroxide | photocatalysis | Z-scheme heterojunctions | environmental chemistry | graphite carbon nitride

Advanced oxidation processes (AOPs) have been widely applied to the treatment of refractory organic pollutants in the environment (1, 2). However, strong oxidants such as hydrogen peroxide (H_2O_2) must be added to generate reactive oxygen species (ROS) for organic pollutant degradation, which results in soaring costs (3). Thus, the application of AOPs is severely restricted, and is scarcely used for in situ restoration of river courses. Moreover, the storage and transportation of strong oxidants pose safety risks (4).

Recently, to reduce costs and avoid danger associated with the storage and transportation, in situ production of H_2O_2 from O_2 reduction and/or H_2O oxidation was proposed as a potential solution (4), which has been realized through electrocatalysis and photocatalysis (5–8). Although the yield of H_2O_2 through electrocatalysis is generally higher than that through photocatalysis, the high energy consumption of electrocatalysis renders its usability for controlling river pollution on site. Conversion of O_2 and H_2O into H_2O_2 through photocatalysis is a promising approach for addressing both the energy crisis and the related environmental problems (Fig. 1A) (5, 9–15). However, due to the rapid recombination of electrons and holes in photocatalysts at picosecond to nanosecond timescales and the weak redox potentials, the dosage of organic electron donors such as methanol and/or the continuous bubbling of pure O_2 are often needed to promote the photocatalytic efficiencies. Nevertheless, the associated high costs and secondary pollution issues are apparently undesirable for on-site restoration of river courses.

The construction of heterojunctions by combining two semiconductors and controlling the electron transfer in a Z-scheme pathway is an invaluable strategy to promote the charge separation efficiency and improve the redox potentials simultaneously. Nevertheless, the construction of Z-scheme heterojunctions remains challenging, as the competitive charge transfer pathway—for example, the type II electron transfer pathway was frequently the dominant pathway, which sacrificed the high redox potentials (Fig. 1B) (16). Recently, the embedded mechanism becomes clear that choosing two constituent semiconductors with a considerable difference between their Fermi levels is an effective strategy for driving the electron transfer in a Z-scheme pathway, which is attributed to the formation of a restrictive internal electric field (16, 17).

By contrast, even when it was demonstrated that Z-scheme heterojunctions could also be constructed from two semiconductors with close Fermi levels, their construction seemed more like trial and error, as it is difficult to predict the electron transfer directions (18, 19). Fortunately, previous studies showed that the prioritized excitation of the reduction semiconductor in a Z-scheme heterojunction resulted in the type II electron transfer pathway, which indicated that the sufficient excitation of the oxidation semiconductor is extremely important in a Z-scheme heterojunction, especially in the visible-light region, since all desirable artificial photosynthesis systems should be used under solar light (18).

Here, to verify our assumption, carbon nitride is selected as the investigation target, as the unmodified carbon nitride cannot be efficiently excited in the visible-light region owing to its weak

Significance

Advanced oxidation processes (AOPs) are widely applied to the treatment of refractory organic pollutants in the environment. However, the continuous addition of oxidant limits their application for in situ remediation of river courses. Hydrogen peroxide (H_2O_2) is the most commonly used oxidant in AOPs. Photosynthesis of H_2O_2 is a promising approach to provide oxidants for AOPs in an in situ and continuous way. However, limited by the rapid charge recombination, organic electron donors and O_2 atmosphere are usually required. Here, a Z-scheme heterojunction photocatalyst achieved the production of H_2O_2 in pure water and open air. The regulation and potential mechanism of the Z-scheme and type II heterojunctions are revealed. This study demonstrates a feasible strategy for developing efficient Z-scheme photocatalysts.
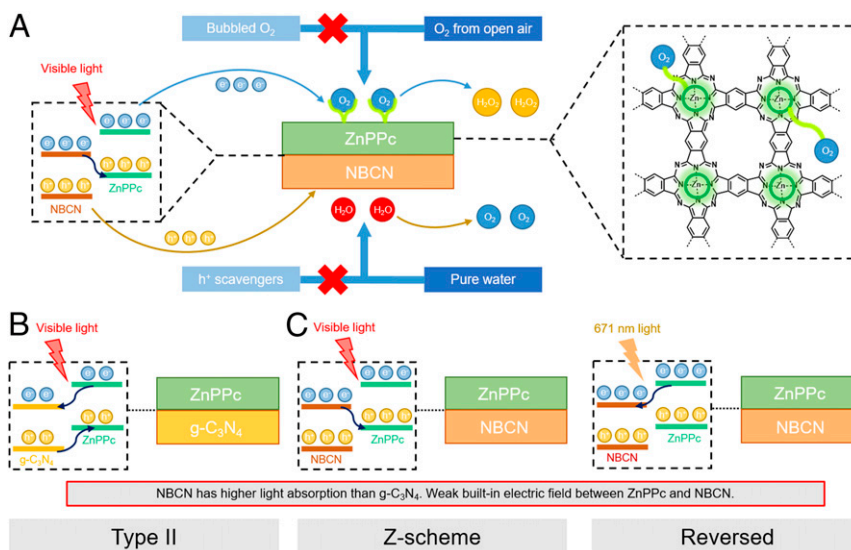
ENGINEERING

Fig. 1. (*A*) Pathways for the photosynthesis of H$_2$O$_2$ from H$_2$O and O$_2$. (*B*) Electron transfer in ZnPPc-g-C$_3$N$_4$ under visible light illumination. (*C*) Electron transfer in ZnPPc-NBCN under visible light or monochromatic light illumination.

absorption in this region. After enhancing its absorption capacity to visible light by doping with boron, a Z-scheme heterojunction is constructed by decorating zinc polyphthalocyanine (ZnPPc) on this modified carbon nitride nanosheets via in situ polymerization, despite the close Fermi levels between ZnPPc and the modified carbon nitride. In comparison, the in situ growth of ZnPPc on unmodified carbon nitride can only produce a type II heterojunction (Fig. 1*B*). To the best of our knowledge, Z-scheme heterojunction has not been previously developed by using any metal poly phthalocyanine and modified carbon nitride. This Z-scheme heterojunction photocatalyst realizes the high-efficient photocatalytic production of H$_2$O$_2$ (114 µmol·g^{-1}·h^{-1}) in pure water and without bubbling pure oxygen, which even outperforms most photocatalysts that require the use of pure O$_2$ (Fig. 1*A*). This study presents a general strategy for constructing Z-scheme heterojunctions when the Fermi-levels of the two constituent semiconductors are close (Fig. 1*C*) and paves an important step for the rational design of Z-scheme heterojunctions.

Results

Configuration and Composition of the Photocatalysts. To increase the visible-light absorbance of carbon nitride, the modified carbon nitride termed as NBCN was prepared by simply calcining the mixture of commercial graphic carbon nitride (g-C$_3$N$_4$) and sodium borohydride (NaBH$_4$) in nitrogen atmosphere at 400 °C, which was subsequently exfoliated by sonication and frozen drying (Fig. 2*A*) (20). As shown in *SI Appendix*, Fig. S1, the characteristic powder X-ray diffraction (PXRD) peak at 27.4° was weakened for NBCN compared with that of the pristine g-C$_3$N$_4$, thereby suggesting the loss of ordered structures within the g-C$_3$N$_4$ framework (21). Another characteristic peak at 13.0° disappeared for NBCN, which indicated that the in-plane ordering structure of the heptazine units was severely distorted (22).

Still, the characteristic heptazine structural backbones of g-C$_3$N$_4$ were observed in the Fourier transform infrared (FTIR) spectrum of NBCN (*SI Appendix*, Fig. S2). Meanwhile, a new absorption band appeared at 2,180 cm^{-1}, which corresponded to the asymmetric stretching vibration of the cyano groups and implied the introduction of cyano groups into NBCN (20). The nitrogen vacancies were verified via elemental analysis (*SI Appendix*, Table S1), as the ratio of the content of C atoms to N atoms in NBCN (0.57) was slightly higher than that in g-C$_3$N$_4$ (0.55). The nitrogen defects (nitrogen vacancies and cyano groups) may be

caused by the active H$_2$ from the thermal decomposition of NaBH$_4$, which reacted with the lattice nitrogen atoms in g-C$_3$N$_4$ to produce NH$_3$ (20, 23).

The successful doping of boron atoms into NBCN was demonstrated by the B1s photoelectron spectroscopic (XPS) signals at 190.51 and 192.08 eV (*SI Appendix*, Fig. S3), which were attributed to the doping at two different sites (20). The B content in NBCN was detected to be 0.09% via the elemental analysis. The morphology of NBCN was also characterized via SEM and AFM (*SI Appendix*, Figs. S4 and S5). NBCN was detected to have a blocky structure with irregular planes, and its roughness (58.2 nm) exceeded that of pristine g-C$_3$N$_4$ (26.7 nm).

Subsequently, ZnPPc-NBCN was synthesized via polymerization of 1,2,4,5-tetracyanobenzene (TCNB) with ZnCl$_2$ in the presence of NBCN that was dispersed in isoquinoline (Fig. 2*A*). The successful decorating of ZnPPc was observed through a color change from yellow to green. The Zn contents in the hybrids were modulated by controlling the amounts of zinc and TCNB during synthesis. The loaded Zn, which was determined via inductively coupled plasma mass spectrometry (ICP-MS), could be controlled in the range from 0.7 µmol to 10 µmol Zn per gram of catalyst (*SI Appendix*, Table S2). The higher Zn content caused a visible intensification of the green color of the catalyst.

Moreover, the diffuse reflectance UV/Vis spectrum (DRS) of ZnPPc-NBCN showed the characteristic (S$_o$→S$_1$) Q band of ZnPPc at 710 nm, which was redshifted compared to that of monomeric ZnPc (*SI Appendix*, Fig. S6) (24). The Urbach tail of ZnPPc-NBCN, which were caused by the loading of ZnPPc on NBCN, could enable the utilization of a broader spectrum of visible light (Fig. 2*B*) (18, 19, 25). The coordination environment of Zn was characterized via XPS (Fig. 2*C*). The Zn 2p spectrum of ZnPPc-NBCN was consisted of peaks at 1,044.6 and 1,021.4 eV, which were attributed to the Zn 2p$_{1/2}$ and Zn 2p$_{3/2}$ transitions, respectively, and was consistent with the corresponding region of pure ZnPPc (1,044.6 and 1,021.5 eV). The small displacement of the Zn 2p signal suggested a weak built-in electric field between ZnPPc and NBCN. The Zn signal could not be detected in the XPS spectrum of Zn-NBCN (following the same synthesis procedure as ZnPPc-NBCN without using the precursor of PPc), which indicated that zinc cations could not be decorated on NBCN. Thus, according to the DRS and XPS signals, Zn in ZnPPc-NBCN was coordinated in the same form as Zn in ZnPPc.
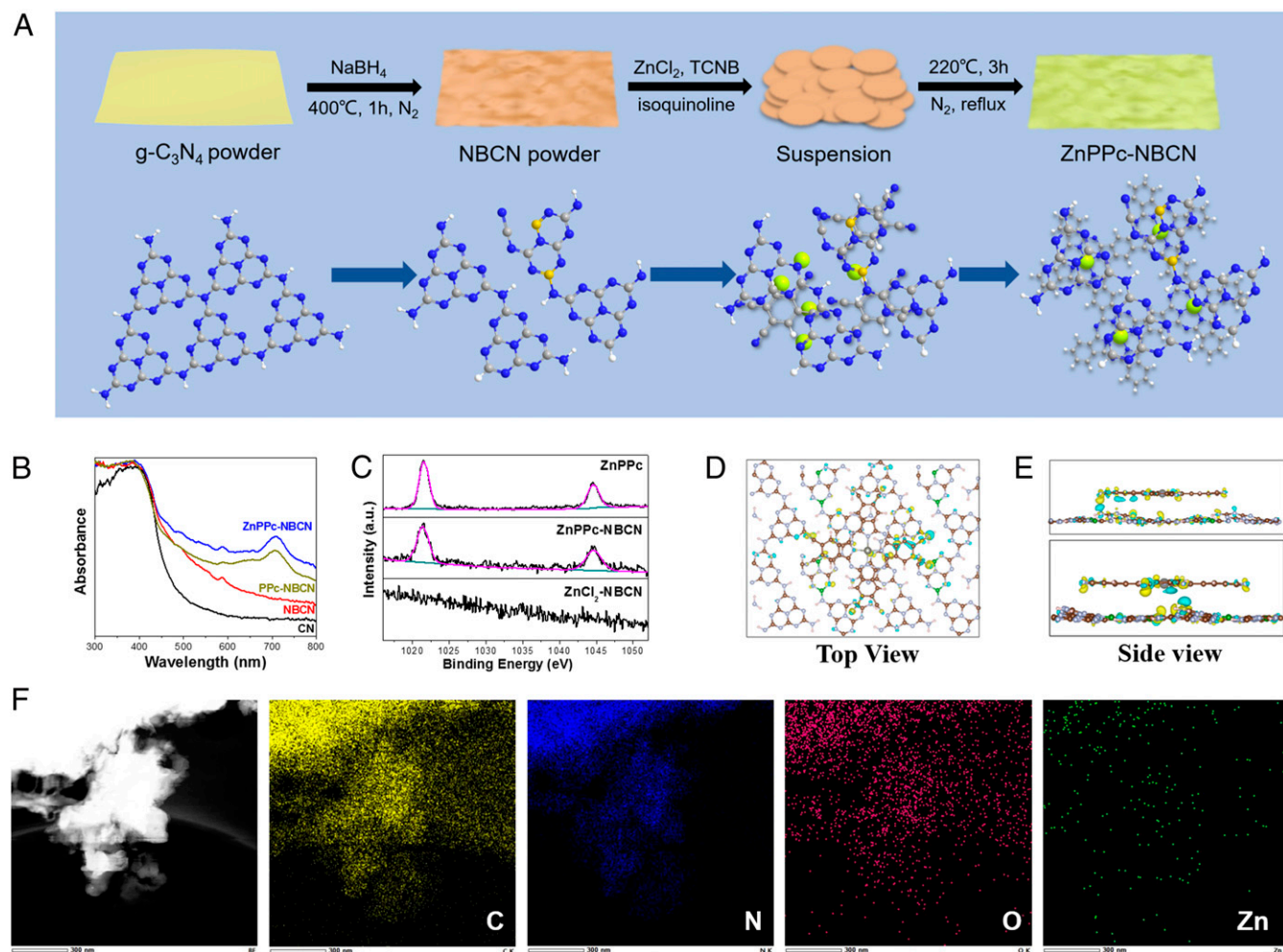
Fig. 2. (A) Schematic illustration of the preparation process of ZnPPc-NBCN and the corresponding DFT-optimized structures. (B) UV-DRS spectras of ZnPPc-NBCN, PPc-NBCN, NBCN, and CN. (C) High-resolution Zn XPS spectra of ZnPPc, ZnPPc-NBCN, and ZnCl₂-NBCN. (D and E) The top view and side view of the electron clouds in ZnPPc-NBCN. (F) Elemental mapping images of ZnPPc-NBCN.

After being hybridized with ZnPPc, the microstructure and functional groups of NBCN were maintained, as demonstrated in the PXRD and FTIR spectra (*SI Appendix*, Figs. S1 and S2). Energy-dispersive X-ray (EDX) analysis of ZnPPc-NBCN demonstrated the uniform distribution of Zn atoms throughout the material (Fig. 2*F*). However, ZnPPc and NBCN could not be distinguished in the transmission electron microscopic (TEM) image (*SI Appendix*, Fig. S4), as both of them were two-dimensional nanomaterials.

To elucidate the microscopic structures of NBCN and ZnPPc-NBCN, DFT calculations were conducted via the hybrid functional method of Perdew–Burke–Ernzerhof (PBE) and Heyd–Scuseria–Ernzerhof (HSE06) (Fig. 2 *D* and *E*), and the reliability of the simulated structures was evaluated by comparing the calculated bandgaps with the experimental data (*SI Appendix*, Fig. S7). The calculated band gap of g-C₃N₄ was 2.52 eV, which was consistent with the experimental value (2.51 eV). DFT calculation demonstrated that the nitrogen-defective g-C₃N₄ with B atoms doped at only one kind of site showed a significantly reduced band gap (2.01 eV and 2.40 eV for the two different doping sites). However, when B atoms were doped at both of the two kinds of sites in the nitrogen-defective g-C₃N₄, the bandgap (2.50 eV) was nearly the same as the experimental value (2.48 eV).

DFT calculations were also conducted to investigate the polymerization degree of ZnPPc on NBCN (*SI Appendix*, Fig. S8).

The experimental band gap of ZnPPc in NBCN was 1.58 eV, which was between the calculated values of the monomer (1.66 eV) and tetramer (1.10 eV) of zinc phthalocyanine. This demonstrated the low polymerization degree of ZnPPc. Furthermore, the simulated charge difference analysis of ZnPPc-NBCN showed that the N atoms in NBCN lose electrons (yellow cloud) and the Zn atoms and the phthalocyanine ring in ZnPPc gain electrons (blue cloud), thereby providing a direct evidence for the charge transfer tendency from NBCN to ZnPPc along the interfacial layer. This charge transfer tendency was also consistent with the XPS spectrum of ZnPPc-NBCN (Fig. 2*C*), which indicated that there existed a weak built-in electric field between ZnPPc and NBCN.

Thermodynamic Feasibility of ZnPPc-NBCN for O₂ Reduction and H₂O Oxidation. ZnPPc-NBCN displayed a stronger absorption for visible light than NBCN, which is ascribed to the high light-harvesting capacity of the phthalocyanine macrocycle (Fig. 2*C*) (26). As shown in *SI Appendix*, Fig. S9, the absorption band edges of ZnPPc in ZnPPc-NBCN, ZnPPc-NBCN, and NBCN were 776, 493, and 500 nm, which corresponded to band gaps of 1.60, 2.52, and 2.48 eV, respectively. Furthermore, the positions of the conduction bands (CBs) were estimated by measuring the flat-band potential (E$_{fb}$) via Mott–Schottky plots. As shown in *SI Appendix*, Fig. S10, the positive slopes of the plots indicated the n-type nature of NBCN, ZnPPc,

and ZnPPc-NBCN, and the E_{fb} values were evaluated as −1.08 V, −1.2 V, and −1.2 V versus the Ag/AgCl electrode [−0.47, −0.59, and −0.59 V versus reversible hydrogen electrode (RHE)] (27, 28). Since the E_{fb} of n-type semiconductors was considered to be 0.1 to 0.2 V below the CB minima (CBM), the CBMs of NBCN, ZnPPc, and ZnPPc-NBCN were estimated to be approximately −0.57 V, −0.69 V, and −0.69 V versus RHE, respectively. In consideration of the aforementioned band gap values, the valence band maxima (VBM) of NBCN, ZnPPc, and ZnPPc-NBCN were calculated to be 1.91 V, 0.9 V, and 1.83 V (Fig. 3A). Thus, considering the redox potential of O_2/H_2O_2 (+0.68 V versus RHE) and O_2/H_2O (+1.23 V versus RHE), both NBCN and ZnPPc-NBCN had strong thermodynamic driving forces to realize O_2 reduction and H_2O oxidation reactions simultaneously (29).

Remarkably, in ZnPPc-NBCN, the desired high redox potentials were maintained, which suggested ZnPPc and NBCN were the reduction and oxidation poles, respectively, in ZnPPc-NBCN.

Photocatalytic Performance of ZnPPc-NBCN in Overall H_2O_2 Production.
The thermodynamic feasibility was further verified by experiment. The photocatalytic activity of ZnPPc-NBCN was evaluated in pure water under the ambient O_2 concentration and without any additives (sacrificial organic electron donors or pH adjustments). Visible light (100 mW cm^{-2}, λ > 400 nm) was used to drive the photocatalytic reactions. As shown in Fig. 3B, ZnPPc-NBCN exhibited a H_2O_2 production rate of as high as 114 μmol·g^{-1}·h^{-1}. By sharp contrast, the bare NBCN generated only trace amounts of H_2O_2 (2 μmol·g^{-1}·h^{-1}), which highlighted the vital role of ZnPPc loaded on NBCN in determining the photocatalytic efficiency (Fig. 3B). Moreover, ZnPPc-NBCN containing 1.5 μmol Zn per gram of the catalyst showed the highest activity in the production of H_2O_2 (Fig. 3B). Thus, without specification, the ZnPPc-NBCN mentioned below refers to the one containing 1.5 μmol·g^{-1} of Zn.

Furthermore, to elucidate the role of ZnPPc in depth, we deliberately selected two analogous photocatalysts, namely, PPc-NBCN (following the same synthesis procedure as ZnPPc-NBCN without using ZnCl$_2$, the successful loading of PPc was demonstrated via DRS, as shown in Fig. 2C) and Zn-NBCN (the loading amount of Zn was 0.70 μmol·g^{-1}, which was demonstrated via ICP-MS, *SI Appendix*, Table S2) for comparison. As shown in Fig. 3B, both of them displayed significantly lower activities toward H_2O_2 generation, namely, 6 μmol·g^{-1}·h^{-1} for PPc-NBCN and 12 μmol·g^{-1}·h^{-1} for ZnCl$_2$-NBCN. These results unequivocally demonstrated that the Zn atoms coordinated to phthalocyanine were the active centers for the reduction of O_2 into H_2O_2 under the ambient O_2 concentration. Moreover, there are two different reduction routes for transforming oxygen into hydrogen peroxide—the direct route and the superoxide radical mediated route. To resolve the exact route, 5,5-dimethyl-pyrroline N-oxide (DMPO) was used as a radical spin-trapping agent in electron paramagnetic resonance (EPR) measurements to examine the existence of superoxide radical during oxygen reduction.

As shown in the *SI Appendix*, Fig. S11, no signal for superoxide radical was detected, which indicated oxygen was directly reduced into hydrogen peroxide.

Notably, the H_2O_2 production rate with catalysis by ZnPPc-NBCN was not influenced by replacing the air above the reaction solution with pure O_2, which demonstrated that it was even not necessary to use pure O_2 in the present photocatalytic system, as the reduction rate of O_2 was supposed to be relative fast in comparison with the oxidation rate of H_2O.

To further identify the product of water oxidation, an RRDE experiment was conducted in a N_2 atmosphere (30). As shown in *SI Appendix*, Fig. S12, the currents in the ring electrode indicated that O_2 and not H_2O_2 was the main product of water oxidation by ZnPPc-NBCN. Thus, as shown in Fig. 1A, O_2 that was evolved from oxidized water could be used to produce H_2O_2, in addition to O_2 from air. Moreover, benefitting from the efficient hole reaction for water oxidation, the use of sacrificial organic electron donors could be avoided. Furthermore, the O_2 evolution rate of ZnPPc-NBCN was as high as 242 μmol·g^{-1}·h^{-1} with NaIO$_3$ as the electron scavenger, which was ten times that of NBCN (24 μmol·g^{-1}·h^{-1}) and ranked one of the best among the reported photocatalysts (20). The high O_2 evolution activity of ZnPPc-NBCN was also demonstrated by the linear sweep voltammetry (LSV) curve, as a lower overpotential and a higher electrical current were presented compared to those of NBCN (*SI Appendix*, Fig. S12), which should be attributed to the higher charge separation efficiency in ZnPPc-NBCN.

To the best of our knowledge, the H_2O_2 production rate with catalysis by ZnPPc-NBCN is the highest among the reported photocatalysts under the same conditions (visible light, room temperature, air atmosphere, and without hole scavengers), and ZnPPc-NBCN is even comparable to the best photocatalysts used in pure oxygen atmosphere (*SI Appendix*, Table S3). Additionally, ZnPPc-NBCN exhibited reproducible activities for five cycles after loading on glass sheet (*SI Appendix*, Fig. S13). It was demonstrated that the functional groups and microstructure could be maintained after being used for five cycles (*SI Appendix*, Fig. S14).

Exploration of Charge Transfer Pathways and a Regulatory Strategy.
To gain deep insight into the charge transfer behaviors at the atomic level in ZnPPc-NBCN, the migration pathway of photogenerated electron-hole pairs between the two components of ZnPPc-NBCN was investigated by in situ XPS spectroscopy (Fig. 4 and *SI Appendix*, Fig. S15) under white light LED illumination (Fig. 4 A and B) (16, 28). The in situ XPS spectroscopy acts as one of effective tools to reveal the flow directions of electrons. In situ XPS measurements were performed in both periods of darkness and irradiation. For the detection of Zn atoms, scanning was repeated for 100 times due to its low content. In situ XPS recorded the shifts of the binding energies. A decrease in binding energy indicated an increase in electron cloud density, and the corresponding atoms were the electron acceptors. The illumination lasted for 23 min
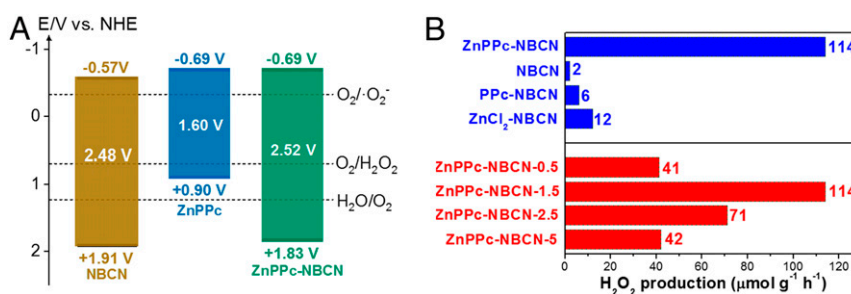

Fig. 3. (A) Band structures of NBCN, ZnPPc, and ZnPPc-NBCN. (B) The top portion represents production rates of H_2O_2 catalyzed by ZnPPc-NBCN, NBCN, PPc-NBCN, and ZnCl$_2$-NBCN; the bottom portion represents ZnPPc-NBCN (ZnPPc-NBCN-x; x indicates x μmol Zn per gram of catalyst).

and was repeated for three successive times. As shown in *SI Appendix*, Fig. S15, all the XPS spectra were calibrated by referring to the C1 peak at 284.7 eV before illumination. The high-resolution Zn XPS spectra of pure ZnPPc-NBCN could be fitted to 1,021.4 eV, which could be assigned to the $2p_{3/2}$ state of Zn (Fig. 2C). For comparison, the XPS spectrum of ZnPPc-NBCN was also recorded without the illumination of white light LED (Fig. 4 C and D and *SI Appendix*, Fig. S15 A and B). The time interval was also 23 min between every two successive records.

When the ZnPPc-NBCN composite was under white light LED illumination, the binding energy (1,201.6 eV) of Zn was increased by 0.2 eV (Fig. 4 E and F). In comparison, when there was no white light LED illumination, the binding energy of Zn was increased by 0.3 eV (Fig. 4 C and D), which should be attributed to the signal shifts triggered by the X-ray irradiation that caused the decomposition of the photocatalyst. Very remarkably, the much lower increment of the binding energy under illumination suggested that the Zn atoms were the electron acceptors under illumination (Fig. 4C). The electron accepting roles of the Zn atoms under illumination were more clearly observed in ZnPPc-NBCN-10 (containing 10 μmol g^{-1} of Zn, Fig. 4 G and H). The binding energy of the Zn atom in ZnPPc-NBCN-10 under illumination was even decreased from 1,021.3 to 1,021.2 eV, in sharp contrast to that without illumination.

The variation of chemical states of the C and N element of ZnPPc-NBCN was within the margin of error no matter with or without illumination (*SI Appendix*, Fig. S15). All these XPS results demonstrated the electron transfer from the NBCN component to the ZnPPc component through the interface between them, when both of these components were excited under white-light LED illumination. In combination with the aforementioned energy levels (Fig. 3A), it could be concluded that a Z-scheme migration pathway of the photoelectrons was verified. The Z-scheme led to electron harvesting on the Zn atoms of ZnPPc for O_2 reduction (Fig. 1A). These results were also consistent with the simulated results obtained via DFT calculations (Fig. 2E).

Moreover, during the test in darkness, the peaks of the triazine structure that corresponded to carbon nitride attenuated substantially (*SI Appendix*, Fig. S15 C and D), and the nitrogen to carbon ratio decreased concurrently (*SI Appendix*, Table S4). These observations are attributed to the cleavage of the triazine bond and the formation of an N vacancy during the test, which were supposed to be caused by X-ray irradiation during the test.

Thereafter, the high charge separation efficiency was also proven via in situ electron paramagnetic resonance (EPR) spectrometry and Kelvin probe force microscopy (KPFM). As shown in *SI Appendix*, Fig. S16, the EPR result (g = 1.998) of ZnPPc-NBCN significantly exceeded that of NBCN, suggesting a higher concentration of unpaired electrons could be maintained in ZnPPc-NBCN (20). After light irradiation, ZnPPc-NBCN exhibited a substantially enhanced EPR signal compared to NBCN, thereby demonstrating the highly efficient photogeneration of electrons and holes in ZnPPc-NBCN. To further identify surface charge modulation, KPFM was employed to analyze the surface
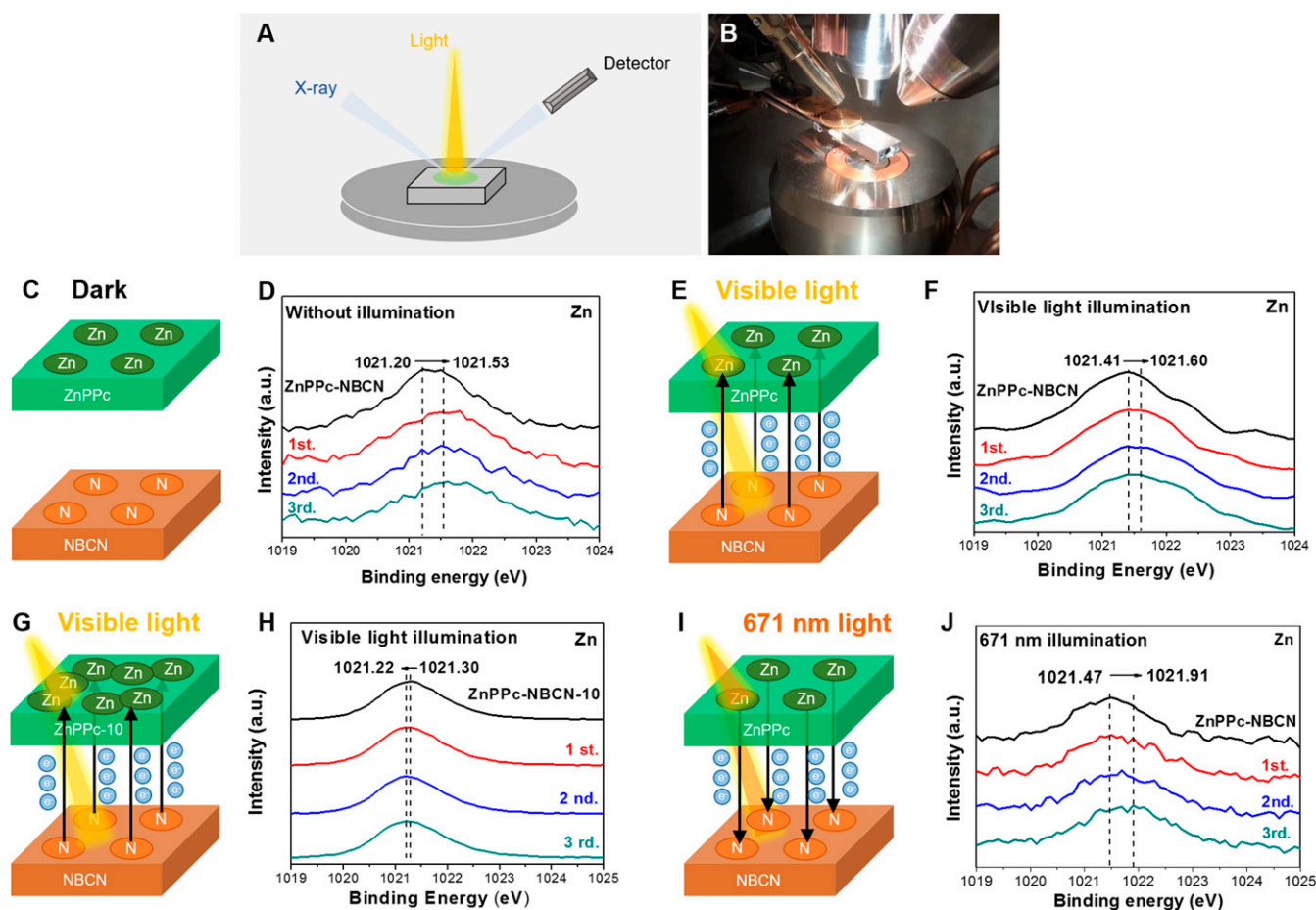

Fig. 4. (*A* and *B*) Schematic illustration and photograph of in situ XPS. (*C* and *D*) Intrinsic state of ZnPPc-NBCN in darkness. (*E* and *F*) Electrons transfer from NBCN to ZnPPc under visible light illumination. (*G* and *H*) Electrons transfer from NBCN to ZnPPc under visible light illumination, even a higher amount of ZnPPc was loaded on NBCN. (*I* and *J*) Electrons transfer from ZnPPc to NBCN under 671 nm illumination.

Ye et al.
Highly efficient photosynthesis of hydrogen peroxide in ambient conditions

PNAS | 5 of 8
https://doi.org/10.1073/pnas.2103964118

potentials at nanometer-scale resolution (*SI Appendix*, Fig. S17) (31). The light-induced contact potential difference (CPD) is directly related to the surface photovoltages (SPVs), increased from NBCN (20 mV) to ZnPPc-NBCN (40 mV). The larger CPD on ZnPPc-NBCN implied the enhanced accumulation of holes on the surface, which demonstrated the more efficient charge separation in ZnPPc-NBCN that was attributed to its Z-scheme heterojunction structure (32).

Furthermore, the work functions of ZnPPc-NBCN and NBCN were also obtained via KPFM. The work function is an important physical parameter for determining the energy level alignments and charge transfer directions for heterojunction structures (33). The work function of ZnPPc was determined to be 0.019 eV smaller than that of NBCN by using the work function of indium tin oxide (ITO) as the comparison mediate (*SI Appendix*, Fig. S18). In other words, the Fermi level of ZnPPc was 0.019 eV higher than that of NBCN. This small difference between the Fermi Levels was responsible for the aforementioned weak built-in electric field in ZnPPc-NBCN, which also suggested the present Z-scheme heterojunction was not the so-called S-scheme heterojunction, as the built-in electric field was not strong enough.

The mechanisms behind the succeeded construction of the Z-scheme ZnPPc-NBCN heterojunction were intriguing, as most of the reported composites of metal phthalocyanine and carbon nitride are type II heterojunctions (Fig. 1*B*) (25, 26, 34–36). To examine this, ZnPPc-CN (CN representing the commercial g-C$_3$N$_4$) was synthesized and well characterized for comparison. As shown in *SI Appendix*, Fig. S19, the CBMs of CN and ZnPPc-CN were both −0.54 eV. In addition, the work function of CN was nearly the same as that of NBCN (0.003 eV higher than the work function of ITO, *SI Appendix*, Fig. S18), thereby suggesting that CN possessed nearly the same Fermi level as NBCN. However, the CBM of ZnPPc-CN was much more positive than that of ZnPPc-NBCN. Hence, ZnPPc-CN was supposed to have a type II heterojunction structure (Fig. 1*B*). The differences between ZnPPc-NBCN and ZnPPc-CN were further investigated. The loading amount of Zn was 1.5 μmol·g^{-1} for ZnPPc-NBCN and 24.4 μmol·g^{-1} for ZnPPc-CN, even though the same amount of ZnCl$_2$ was used for the synthesis (*SI Appendix*, Table S2). The high loading amount of ZnPPc for ZnPPc-CN was also proven by DRS (*SI Appendix*, Fig. S20), as the Q band of ZnPPc was more significantly redshifted. To explore the influence of the loading amount of Zn on the heterojunction type, ZnPPc-NBCN-10 was also synthesized and characterized (*SI Appendix*, Table S2). In situ XPS demonstrated that the electron transfer in ZnPPc-NBCN-10 was still in a Z-scheme pathway (Fig. 4*D* and *SI Appendix*, Fig. S15 *E* and *F*), which indicated that the loading amount of ZnPPc was not the reason for the formation of different heterojunctions.

On the other hand, NBCN showed much stronger absorption in the visible light region (λ > 400 nm) than CN (Fig. 2*C*). Thus, the influence of light absorption of the two components on the electron migration pathway was investigated. A laser that was centered at 671 nm was used to excite ZnPPc-NBCN (Fig. 4 *I* and *J*), in which ZnPPc had much stronger absorption than NBCN (Fig. 2*B*). At the same time, the electron transfer pathway was characterized via in situ XPS (Fig. 4 *I* and *J*). The binding energy of Zn increased by as high as 0.4 eV (from 1,021.5 eV to 1,022.0 eV, Fig. 4*J*). The chemical state of C and N was almost unchanged (*SI Appendix*, Fig. S15 *G* and *H*). These data strongly suggested that Zn atoms acted as the electron donors. These results demonstrated that the electrons transferred from ZnPPc to NBCN when ZnPPc was more efficiently excited than NBCN (Figs. 1*C* and 4*I*). By contrast, as discussed above, electrons transferred in the opposite direction when the two components were both efficiently excited under white light LED illumination (Figs. 1*C* and 4*E*). Therefore, it could be inferred that the low visible-light absorption of CN was the primary reason for the

formation of the type II ZnPPc-CN heterojunction under visible light illumination. Furthermore, the electron transfer pathway of ZnPPc-NBCN could be regulated in the Z-scheme or type II mode, depending on the illumination conditions.

Discussion

This study demonstrates that the elaborately designed ZnPPc-NBCN is a highly efficient photocatalyst for overall H$_2$O$_2$ production driven by visible light and without consuming pure O$_2$ and organic electron donors. The catalytic activity of ZnPPc-NBCN far exceeds those of reported photocatalysts under the same conditions, and even ranks among the top photocatalysts, regardless of if the continuous bubbling of pure O$_2$ being used or not. On the basis of comprehensive studies on electron transfer pathways, the superior performance of ZnPPc-NBCN is attributed to the Z-scheme heterojunction that formed between ZnPPc and NBCN. To the best of our knowledge, Z-scheme heterojunctions have never been successfully constructed based on any metal polyphthalocyanine and modified carbon nitride. Moreover, a deep investigation that was based on in situ XPS provided insights into the regulatory mechanism for controlling the heterojunction type, which showed that the photoresponse of the components could be used as the driving force to modulate the electron transfer direction in heterojunctions with weak built-in electric fields. This study presents an innovative strategy for improving the photoresponses of oxidation semiconductors to construct an efficient Z-scheme heterojunction under weak built-in electric fields.

Materials and Methods

Preparation of the NBCN. Boron-doped and nitrogen-deficient g-C$_3$N$_4$ (NBCN) was synthesized via reported thermal polymerization method (20).

Typically, 0.4 g g-C$_3$N$_4$ and 0.16 g NaBH$_4$ were ground finely and then calcined at 400 °C in N$_2$ atmosphere for 1 h with a ramping rate of 10 °C/min. After cooled to room temperature, the obtained powders were washed with ethanol and distilled water for several times and dried under vacuum. The products were denoted as NBCN. Afterwards, 500 mg powder was dispersed in 400 mL distilled water and then exfoliated for 6 h in the ice bath. The suspension was then freeze-dried in preparation of the further synthesis.

Preparation of NBCN-ZnPPc-1. NBCN-ZnPPc-1 was synthesized via modified reported method (37). A total of 200 mg exfoliated NBCN, 1,2,4,5-tetra-cyanobenzene (TCNB, 89 mg, 0.5 mmol), and ZnCl$_2$ (34 mg, 0.25 mmol) were dispersed in 150 mL isoquinoline. The dispersion was heated under N$_2$ atmosphere at 200 °C for 3 h. The color of the suspension changed from yellow to pale green. The product was collected by centrifugation and sequentially washed with ethanol, distilled water, and ethanol and dried under vacuum overnight.

Characterization. Powder X-ray diffraction (PXRD) patterns of modificatory CN were collected on a Bruker D8 Advance diffractometer (Cu Kα) at room temperature. X-ray photoelectron spectroscopy (XPS) was performed on an ESCALAB Xi+ spectrometer (Thermo Fisher Scientific). A white light LED lamp or 671 nm laser was used as the light source to obtain the XPS spectra with in situ illumination. The UV-visible (UV-vis) absorbance measurement was performed with a 2800S spectrophotometer (SOPTOP, Shanghai). Fourier transform infrared spectra (FT-IR) were recorded on a PerkinElmer Frontier spectrometer. The morphology images of the catalysts were analyzed by a thermal field emission environmental scanning electron microscope (SEM, Quanta 400F, FEI/OXFORD/HKL). High resolution transmission electron microscopy (HRTEM) and Energy-dispersive X-ray (EDX) spectra were recorded using a JEM-ARM 200P instruments. ICP-MS was carried-out with a Thermo Fisher (ICAP Qc) ICP-MS chemical analyzer. The roughness of the sample was evaluated by using an atomic force microscope (AFM) (Bruker Dimension Fastscan). The surface potential and the working function of the sample were tested by Kelvin Probe Force Microscopy (KPFM) in ambient atmosphere with an AM-KPFM mode. The illumination system was set up with a white-light LED. Electron spin resonance (ESR) signals were recorded with a A300 spectrometer and 300 W Xe lamp was used as light source. For superoxide radical trapper experiment, 5,5-dimethyl-1-pyrroline N oxide (DMPO) was used as the radical trapper and methanol as the solvent.

Electrochemical Measurements. The oxygen reduction reactions (ORR) on NBCN and ZnPPc-NBCN were monitored by using a rotating ring-disk electrode (RRDE) in a three-electrode cell connected to the electrochemical workstation (CHI 760E Instruments). A saturated Ag/AgCl used as a reference, a Pt net as a counter in an electrolyte composed of oxygen-saturated phosphate buffer (pH = 7, 0.1 M). The RRDE that was composed of a glassy carbon disk and a Pt ring was used as a working electrode. Prior to measurements, the catalyst ink was dropped on the glassy carbon disk and dried at room temperature. The number of the transferred electrons was calculated following Eq. **1**:

$$n = \frac{4I_d}{I_d + I_r/N}.$$ **[1]**

The selectivity of H_2O_2 was determined by Eq. **2**:

$$H_2O_2\% = 200 \times \frac{I_r/N}{I_d + I_r/N},$$ **[2]**

in which I_d is the disk current, I_r is the ring current, and N is the collection efficiency.

The oxygen evolution reactions on NBCN and ZnPPc-NBCN were similar to the ORR test method except for the Ar atmosphere instead of pure O_2.

Calculation Methods. All calculations were performed using the Vienna Abinitio Simulation Package (VASP) with the projector augment wave (PAW) method (38, 39). The exchange and correlation potential was described with the PBE of the generalized gradient approximation (GGA). Given the absence of strong bonding interactions between g-C_3N_4 and ZnPPc, the PBE that formed with can der Waals (vdW) correction (PBE-D2) was selected because of its good description of long-range vdW interaction (40). The cutoff energy for electronic wave functions was set to 520 eV. Geometry optimizations were terminated when the energy and force on each ion were reduced below 10^{-6} eV and 0.02 eV/Å, and the optimized structures were then used to calculate the electronic structures. The HSE06 hybrid functional was used to obtain the correct electronic structures of monomer ZnPc and tetramer ZnPPc (41). In the HSE06 functional, the exchange-correlation energy is expressed as

$$E_{XC}^{HSE} = \alpha E_X^{SR}(\mu) + (1 - \alpha)E_X^{PBE,SR}(\mu) + E_X^{PBE,LR}(\mu) + E_C^{PBE}.$$ **[3]**

The charge density difference is defined as follows,

$$\Delta\rho = \rho(NBCN/ZnPC) - \rho(NBCN) - \rho(ZnPc),$$ **[4]**

in which the $\Delta\rho$ is the charge difference between two substrate $\rho(NBCN)$ and $\rho(ZnPc)$. The ρ (NBCN/ZnPc) is the total density of the composite.

Photocatalytic Reaction. The photocatalytic reaction to generate H_2O_2 was performed according to the literature with a slight modification. In photocatalytic H_2O_2 evolution experiment, a specific amount of catalyst was dispersed within 20 mL H_2O in a 50 mL quartz beaker. Prior to photocatalytic testing, the reaction solution was ultrasonic treated for 30 min in the dark to disperse the catalysts. The beaker was then irradiated light simulator with a Xe lamp through a UV cut filter (100 mW/cm², 800 nm > λ > 400 nm) while stirring. At certain time intervals, certain amount of solution was sampled and filtrated with a 0.22 μm Millipore filter to remove the photocatalyst. The reaction was carried out in open air atmosphere in room temperature. If compare the different atmospheres, it needs to bubble O_2 or Ar into the suspension solution for 30 min before measurement. The water oxidation was performed via a controllable reaction system (CEL-SPH2N, CEAULight, China) with a volume of ~100 mL The water oxidation reaction with $NaIO_3$ (2.5 mM) as a sacrificial electron acceptor and La_2O_3 as pH buffer agent was carried out with catalyst (10 mg) in water (20 mL) under Ar atmosphere (1 atm). The O_2 reduction reaction with isopropanol as a sacrificial electron donor was performed with catalyst (10 mg) in a mixture solution of 9:1 H_2O/ isopropanol (vol/vol) (20 mL).

1. L. Zhu *et al.*, Designing 3D-MoS₂ sponge as excellent cocatalysts in advanced oxidation processes for pollutant control. *Angew. Chem. Int. Ed. Engl.* **59**, 13968–13976 (2020).
2. P. Zhou *et al.*, Fast and long-lasting iron(III) reduction by boron toward green and accelerated fenton chemistry. *Angew. Chem. Int. Ed. Engl.* **59**, 16517–16526 (2020).
3. Y. Chen, G. Zhang, H. Liu, J. Qu, Confining free radicals in close vicinity to contaminants enables ultrafast fenton-like processes in the interspacing of MoS₂ membranes. *Angew. Chem. Int. Ed. Engl.* **58**, 8134–8138 (2019).
4. L. Li, Z. Hu, J. C. Yu, On-demand synthesis of H₂O₂ by water oxidation for sustainable resource production and organic pollutant degradation. *Angew. Chem. Int. Ed. Engl.* **59**, 20538–20544 (2020).
5. Y. Shiraishi *et al.*, Resorcinol-formaldehyde resins as metal-free semiconductor photocatalysts for solar-to-hydrogen peroxide energy conversion. *Nat. Mater.* **18**, 985–993 (2019).
6. Q. Chang *et al.*, Promoting H₂O₂ production via 2-electron oxygen reduction by coordinating partially oxidized Pd with defect carbon. *Nat. Commun.* **11**, 2178 (2020).
7. Z. Lu *et al.*, High-efficiency oxygen reduction to hydrogen peroxide catalysed by oxidized carbon materials. *Nat. Catal.* **1**, 156–162 (2018).
8. C. Xia *et al.*, Confined local oxygen gas promotes electrochemical water oxidation to hydrogen peroxide. *Nat. Catal.* **3**, 125–134 (2020).
9. X. Zeng *et al.*, Simultaneously tuning charge separation and oxygen reduction pathway on graphitic carbon nitride by polyethylenimine for boosted photocatalytic hydrogen peroxide production. *ACS Catal.* **10**, 3697–3706 (2020).
10. C. Chu *et al.*, Spatially separating redox centers on 2D carbon nitride with cobalt single atom for photocatalytic H₂O₂ production. *Proc. Natl. Acad. Sci. U.S.A.* **117**, 6376–6382 (2020).
11. Z. Teng *et al.*, Edge-functionalized g-C₃N₄ nanosheets as a highly efficient metal-free photocatalyst for safe drinking water. *Chem* **5**, 664–680 (2019).
12. J. Cai *et al.*, Crafting mussel-inspired metal nanoparticle-decorated ultrathin graphitic carbon nitride for the degradation of chemical pollutants and production of chemical resources. *Adv. Mater.* **31**, e1806314 (2019).
13. Y. Kofuji *et al.*, Carbon nitride-aromatic diimide-graphene nanohybrids: Metal-free photocatalysts for solar-to-hydrogen peroxide energy conversion with 0.2% efficiency. *J. Am. Chem. Soc.* **138**, 10019–10025 (2016).
14. J. M. Campos-Martin, G. Blanco-Brieva, J. L. G. Fierro, Hydrogen peroxide synthesis: An outlook beyond the anthraquinone process. *Angew. Chem. Int. Ed. Engl.* **45**, 6962–6984 (2006).
15. Z. Wei *et al.*, Efficient visible-light-driven selective oxygen reduction to hydrogen peroxide by oxygen-enriched graphitic carbon nitride polymers. *Energy Environ. Sci.* **11**, 2581–2589 (2018).
16. Q. Xu, L. Zhang, B. Cheng, J. Fan, J. Yu, S-scheme heterojunction photocatalyst. *Chem* **6**, 1543–1559 (2020).
17. W. Zhang, A. R. Mohamed, W. J. Ong, Z-scheme photocatalytic systems for carbon dioxide reduction: Where are we now? *Angew. Chem. Int. Ed. Engl.* **59**, 22894–22915 (2020).
18. J. Sun *et al.*, Efficiently photocatalytic conversion of CO₂ on ultrathin metal phthalocyanine/g-C₃N₄ heterojunctions by promoting charge transfer and CO₂ activation. *Appl. Catal. B* **277**, 119199 (2020).
19. J. Bian *et al.*, Dimension-matched zinc phthalocyanine/BiVO₄ ultrathin nanocomposites for CO₂ reduction as efficient wide-visible-light-driven photocatalysts via a cascade charge transfer. *Angew. Chem. Int. Ed. Engl.* **58**, 10873–10878 (2019).
20. D. Zhao *et al.*, Synergy of dopants and defects in graphitic carbon nitride with exceptionally modulated band structures for efficient photocatalytic oxygen evolution. *Adv. Mater.* **31**, e1903545 (2019).
21. X. Wang *et al.*, A metal-free polymeric photocatalyst for hydrogen production from water under visible light. *Nat. Mater.* **8**, 76–80 (2009).
22. H. Yu *et al.*, Alkali-assisted synthesis of nitrogen deficient graphitic carbon nitride with tunable band structures for efficient visible-light-driven hydrogen evolution. *Adv. Mater.* **29** (2017).
23. Y. Wang *et al.*, Linker-controlled polymeric photocatalyst for highly efficient hydrogen evolution from water. *Energy Environ. Sci.* **10**, 1643–1651 (2017).
24. N. Han *et al.*, Supported cobalt polyphthalocyanine for high-performance electrocatalytic CO₂ reduction. *Chem* **3**, 652–664 (2017).
25. X. Zhang *et al.*, Highly asymmetric phthalocyanine as a sensitizer of graphitic carbon nitride for extremely efficient photocatalytic H2 production under near-infrared light. *ACS Catal.* **4**, 162–170 (2013).
26. F. L. Zhang *et al.*, Elucidating molecule-plasmon interactions in nanocavities with 2 nm spatial resolution and at the single-molecule level. *Angew. Chem. Int. Ed. Engl.* **58**, 12133–12137 (2019).
27. Z.-B. Fang *et al.*, Boosting interfacial charge-transfer kinetics for efficient overall CO₂ photoreduction via rational design of coordination spheres on metal-organic frameworks. *J. Am. Chem. Soc.* **142**, 12515–12523 (2020).
28. P. Xia *et al.*, Designing a 0D/2D S-scheme heterojunction over polymeric carbon nitride for visible-light photocatalytic inactivation of bacteria. *Angew. Chem. Int. Ed. Engl.* **59**, 5218–5225 (2020).

Ye et al.
Highly efficient photosynthesis of hydrogen peroxide in ambient conditions

29. H. Hou, X. Zeng, X. Zhang, Production of hydrogen peroxide by photocatalytic processes. *Angew. Chem. Int. Ed. Engl.* **59**, 17356–17376 (2020).

30. L. Chen *et al.*, Acetylene and diacetylene functionalized covalent triazine frameworks as metal-free photocatalysts for hydrogen peroxide production: A new two-electron water oxidation pathway. *Adv. Mater.* **32**, e1904433 (2020).

31. Y. Jiang *et al.*, All-solid-state Z-scheme α-Fe_2O_3/amine-RGO/$CsPbBr_3$ hybrids for visible-light-driven photocatalytic CO_2 reduction. *Chem* **6**, 766–780 (2020).

32. P. Zhang *et al.*, Heteroatom dopants promote two-electron O_2 reduction for photocatalytic production of H_2O_2 on polymeric carbon nitride. *Angew. Chem. Int. Ed.* **59**, 16209–16217 (2020).

33. P. Wang *et al.*, Unraveling the interfacial charge migration pathway at the atomic level in a highly efficient Z-scheme photocatalyst. *Angew. Chem. Int. Ed. Engl.* **58**, 11329–11334 (2019).

34. E. S. Da Silva *et al.*, Novel hybrids of graphitic carbon nitride sensitized with free-base meso-tetrakis(carboxyphenyl) porphyrins for efficient visible light photocatalytic hydrogen production. *Appl. Catal. B* **221**, 56–69 (2018).

35. D. Chen *et al.*, Visible light photoactivity enhancement via CuTCPP hybridized g-C_3N_4 nanocomposite. *Appl. Catal. B* **166-167**, 366–373 (2015).

36. Y. Li, T. Kong, S. Shen, Artificial photosynthesis with polymeric carbon nitride: When meeting metal nanoparticles, single atoms, and molecular complexes. *Small* **15**, e1900772 (2019).

37. S. Roy, E. Reisner, Visible-light-driven CO_2 reduction by mesoporous carbon nitride modified with polymeric cobalt phthalocyanine. *Angew. Chem. Int. Ed. Engl.* **58**, 12180–12184 (2019).

38. G. Kresse, J. Furthmüller, Efficient iterative schemes for ab initio total-energy calculations using a plane-wave basis set. *Phys. Rev. B Condens. Matter* **54**, 11169–11186 (1996).

39. G. Kresse, J. Furthmüller, Efficiency of ab-initio total energy calculations for metals and semiconductors using a plane-wave basis set. Iterative schemes for ab initio total-energy calculations using a plane-wave basis set. *Comput. Mater. Sci.* **6**, 15–50 (1996).

40. S. Grimme, Semiempirical GGA-type density functional constructed with a long-range dispersion correction. *J. Comput. Chem.* **27**, 1787–1799 (2006).

41. J. Heyd, G. E. Scuseria, M. Ernzerhof, Hybrid functionals based on a screened Coulomb potential. *J. Chem. Phys.* **118**, 8207 (2003).